The Astrophysical Journal, 770:112 (8pp), 2013 June 20 doi:10.1088/0004-637X/770/2/112

CARMA MEASUREMENTS OF THE SUNYAEV–ZEL'DOVICH EFFECT IN RX J1347.5−1145

Thomas J. Plagge[1], Daniel P. Marrone[1,2], Zubair Abdulla[1], Massimiliano Bonamente[3,4], John E. Carlstrom[1,5,6], Megan Gralla[1,7], Christopher H. Greer[1], Marshall Joy[4], James W. Lamb[8], Erik M. Leitch[1], Adam Mantz[1], Stephen Muchovej[8], and David Woody[8]
[1] Kavli Institute for Cosmological Physics, Department of Astronomy and Astrophysics, University of Chicago, Chicago, IL 60637, USA
[2] Steward Observatory, University of Arizona, 933 North Cherry Avenue, Tucson, AZ 85721, USA
[3] Department of Physics, University of Alabama, Huntsville, AL 35899, USA
[4] Space Science-VP62, NASA Marshall Space Flight Center, Huntsville, AL 35812, USA
[5] Enrico Fermi Institute, University of Chicago, Chicago, IL 60637, USA
[6] Department of Physics, University of Chicago, Chicago, IL 60637, USA
[7] Department of Physics and Astronomy, Johns Hopkins University, Baltimore, MD 21218, USA
[8] Owens Valley Radio Observatory, California Institute of Technology, Big Pine, CA 93513, USA
Received 2012 March 9; accepted 2013 April 19; published 2013 June 3

ABSTRACT

We demonstrate the Sunyaev–Zel'dovich (SZ) effect imaging capabilities of the Combined Array for Research in Millimeter-wave Astronomy (CARMA) by presenting an SZ map of the galaxy cluster RX J1347.5−1145. By combining data from multiple CARMA bands and configurations, we are able to capture the structure of this cluster over a wide range of angular scales, from its bulk properties to its core morphology. We find that roughly 9% of this cluster's thermal energy is associated with sub-arcminute-scale structure imparted by a merger, illustrating the value of high-resolution SZ measurements for pursuing cluster astrophysics and for understanding the scatter in SZ scaling relations. We also find that the cluster's SZ signal is lower in amplitude than suggested by a spherically symmetric model derived from X-ray data, consistent with compression along the line of sight relative to the plane of the sky. Finally, we discuss the impact of upgrades currently in progress that will further enhance CARMA's power as an SZ imaging instrument.

Key word: galaxies: clusters: general

Online-only material: color figures

1. INTRODUCTION

Galaxy clusters are the largest gravitationally bound systems in the universe and have taken nearly a Hubble time to form. They therefore have the potential to act as powerful probes of cosmology if systematic errors can be controlled. Precision cluster cosmology will require a deep understanding of cluster astrophysics, particularly as it relates to the hot gas of the intracluster medium (ICM). So far, the most detailed studies of the ICM have been performed by X-ray telescopes, which are sensitive to the bremsstrahlung emission from the 10^7–10^8 K gas. The Sunyaev–Zel'dovich (SZ) effect is a complementary probe of the ICM. The amplitude of the SZ signal depends on the line-of-sight integral of the ICM pressure (the product of density n_e and temperature T), while the X-ray surface brightness depends on n_e^2, so sensitive SZ measurements can access tenuous gas outside the cluster core and directly measure pressure disturbances. Features found commonly in the outer regions of clusters, such as shocked gas from mergers, may therefore be easier to detect using the SZ effect than using X-rays. Moreover, the combination of X-ray and SZ data can be used to obtain a more complete picture of the ICM thermodynamics.

To take advantage of these opportunities, advances in SZ imaging capabilities are needed. Measurements of the SZ effect have become routine over the last decade, but the full potential of the SZ effect as a probe of cluster physics remains largely unexploited due to technical challenges: the combination of high sensitivity and large angular dynamic range required for detailed SZ imaging has proven difficult to achieve with existing instruments. As a result, the use of the SZ effect has been limited primarily to studies where resolved imaging is unnecessary.

The small number of higher-resolution SZ images obtained to date have served to demonstrate the utility of the technique. However, single-dish measurements such as those by Korngut et al. (2011) can suffer from radio point source contamination and have been limited to scales $<45''$ by the necessity of filtering out modes contaminated by atmospheric noise. Multi-dish SZ measurements by arrays such as the Australia Telescope Compact Array (e.g., Malu et al. 2010) can constrain and remove point sources using the inherent spatial filtering ability of interferometers, but most millimeter-wave interferometers lack sensitivity at arcminute angular scales where the SZ cluster signal is largest.

The Combined Array for Research in Millimeter-wave Astronomy (CARMA) is a heterogeneous interferometric array consisting of 23 antennas with diameters of 3.5, 6.1, and 10.4 m operating at 1 cm, 3 mm, and 1 mm. This particular combination of antennas and bands makes CARMA a uniquely powerful SZ instrument: its 3.5 m antennas can be placed in a compact configuration sensitive to arcminute-scale emission, and its 6.1 and 10.4 m dishes can be used to obtain the sensitivity necessary to resolve smaller angular scale SZ features. Furthermore, the large telescopes provide a simultaneous measurements at high sensitivity and angular resolution of any contaminating emission from radio bright galaxies; this emission can then be removed with high dynamic range from the low-brightness SZ signal. In this work, we make use of CARMA data from three array configurations and two bands to obtain an SZ image of the galaxy cluster RX J1347.5−1145. These data represent the highest-fidelity picture of a galaxy cluster ever obtained using the SZ effect.

This paper is organized as follows. Section 2 provides background on RX J1347.5−1145, Section 3 describes the

observations and data reduction, and Section 4 discusses the modeling and deconvolution method. We present our results and compare them to previous measurements in Section 5, and review the conclusions and discuss prospects for future work in Section 6.

2. RX J1347.5−1145

The target for these observations is the cluster RX J1347.5−1145, an object that has been characterized extensively using a variety of techniques. First discovered by the *ROSAT* all-sky survey (Voges et al. 1999), RX J1347.5−1145 is one of the most luminous clusters in the X-ray sky, and has been measured by several X-ray instruments including *Chandra* (Allen et al. 2002) and *XMM-Newton* (Gitti & Schindler 2004). Optical observations have revealed the presence of two cD galaxies, one coincident with the X-ray emission peak and one directly to the east (Bradač et al. 2008; Cohen & Kneib 2002; Johnson et al. 2011). The system has also been found to host a radio mini-halo (Gitti et al. 2007). Its gravitational potential has been probed using both strong and weak gravitational lensing (e.g., Miranda et al. 2008; Bradač et al. 2008). These multi-wavelength observations indicate that RX J1347.5−1145 is a massive ($>10^{15}$ $M_{\odot}$) cluster at redshift $z = 0.4510$ which has recently undergone a merger with a smaller object. The cluster's SZ signal has been measured using single-dish (Pointecouteau et al. 1999; Komatsu et al. 2001; Kitayama et al. 2004; Mason et al. 2010; Korngut et al. 2011) and interferometric (Carlstrom et al. 2002; Bonamente et al. 2008, 2011) imaging instruments, and its spectrum near the thermal SZ null has also been characterized (Zemcov et al. 2012). The higher angular resolution measurements have revealed a compact region of very hot (∼20 keV) gas to the southeast of the X-ray emission peak, while the low-resolution data indicate a lower-amplitude arcminute-scale SZ signal than suggested by a spherical fit to the X-ray data.

The existence of a central radio-bright active galactic nucleus, along with the limited angular dynamic range of most SZ instruments, has complicated efforts to bring SZ data to bear on understanding this system. The CARMA data we present help to overcome both limitations.

3. OBSERVATIONS AND DATA REDUCTION

RX J1347.5−1145 was observed with three different sets of CARMA antennas at two wavelengths: an 8 element sub-array consisting of 3.5 m antennas at 1 cm ("CARMA-8"), a 15 element sub-array consisting of 6.1 m and 10.4 m antennas at 3 mm ("CARMA-15"), and the full 23 element array at 3 mm ("CARMA-23").

The CARMA-8 data were obtained in 2009 August. A series of data quality cuts was applied to the data, most notably based on antenna shadowing and irregular system temperatures; as is typical for such observations, these cuts flagged approximately 25% of the data. A total of 25.7 hr of unflagged on-source time was obtained. The center frequency was 31 GHz with a bandwidth of 8 GHz, and the target R.A. and decl. were 13:47:30.7 and −11:45:08.6 in J2000 coordinates. The array was configured with six elements in a compact array sensitive to arcminute-scale SZ signals, and two outlying elements providing simultaneous discrimination for compact radio source emission. The compact array and longer baselines sample uv-spacings of 350–1300λ and 2–7.5 kλ, respectively. The data were reduced using the Sunyaev–Zel'dovich Array (SZA) pipeline described in Muchovej et al. (2007).

The CARMA-15 data were obtained in 2010 July and totaled 7.4 hr of unflagged, on-source time. The center frequency was 90 GHz with a bandwidth of 8 GHz, and the target R.A. and decl. were 13:47:32.0 and −11:45:42.0 in J2000 coordinates. The CARMA-15 array was pointed slightly southeast of the CARMA-8 phase center, directly toward the region of hot gas. The antennas were in the E configuration, the most compact standard positions for the 6.1 and 10.4 m antennas with baseline lengths ranging from 8 to 66 m. Data reduction was performed using MIRIAD (Sault et al. 1995).

We obtained CARMA-23 data as part of a commissioning run in 2011 February. All 23 antennas were operated at a center frequency of 86 GHz and were attached to the CARMA spectral line correlator, which operated at a reduced bandwidth—4 GHz for the double-sideband receivers on the 10.4 and 6.1 m antennas, and 2 GHz for the single-sideband receivers on the 3.5 m antennas. A total of 8.6 hr of unflagged on-source data were obtained; a relatively high fraction of the 3.5 m data were flagged due to hardware issues in the commissioning run that have since been corrected. The array configuration was approximately the combined CARMA-8 and CARMA-15 configurations, with baselines varying from 4 to 66 m. The target R.A. and decl. were the same as for CARMA-8 rather than the offset coordinates used for CARMA-15. The longer-baseline CARMA-23 data therefore complements the CARMA-15 data by making the sensitivity at small angular scales roughly uniform over a region encompassing both the cluster core and the region of disturbed gas. We reduced the CARMA-23 data using MIRIAD.

For the CARMA-15 and CARMA-23 arrays, we treat each baseline type (10.4 m × 10.4 m, 10.4 m × 6.1 m, etc.) separately to properly account for the differing primary beams. We therefore have 10 data sets: 1 for CARMA-8, 3 for CARMA-15, and 6 for CARMA-23. We apply a cutoff in uv radius for each data set, using the data beyond the cutoff only to constrain the point source emission. The cutoff is chosen to exclude portions of the uv plane which are poorly sampled for a given baseline type.

The outputs of the data reduction pipelines consist of flagged, calibrated visibilities $V(u,v)$. All absolute flux calibration is performed using the Rudy (1987) Mars model, and is accurate to 5%. To combine data from different bands, we define $y(u,v)$, the Fourier-space counterpart to the Compton y parameter (Carlstrom et al. 2002):

$$y(u, v) \equiv \frac{V_{\nu}(u, v)}{g(\nu, T_{\rm e})\, I_0} \quad (1)$$

where $g(\nu, T_{\rm e})$ is the relativistic frequency and temperature dependence of the SZ signal, $I_0 = 2(k_B T_{\rm CMB})^3/(hc)^2$, and $T_{\rm e}$ is the ICM electron temperature. Due to our incomplete knowledge of the true electron temperature as a function of position within the cluster, we approximate the temperature dependence by calculating $g(\nu, T_{\rm e})$ at the 12 keV temperature which best fits the *Chandra* data (Allen et al. 2002). The relative value of $g(\nu, T_{\rm e})$ between 1 cm and 3 mm is nearly independent of $T_{\rm e}$, varying by just 2% between 5 and 15 keV.

The 10 $y(u,v)$ data sets are summarized in Table 1, and the dirty maps are shown in Figure 1. The data weight distribution in the uv plane for the combined data sets is shown in Figure 2. To illustrate the contributions of each of the three sub-arrays, we show the measured $y(u,v)$ binned in uv radius in Figure 3.

Table 1
CARMA Observations of RX J1347.5−1145

Array	Ant 1 Diam (m)	Ant 2 Diam (m)	Frequency (GHz)	uv Cutoff (kλ)	Noise (mJy beam^{-1})	Minor Axis (arcsec)	Major Axis (arcsec)	Beam P.A. (deg)	Primary Beam FWHM (arcsec)
CARMA-8	3.5	3.5	31	2	0.16	100	130	−33	630
CARMA-15	10.4	10.4	90	10	0.38	13	17	73	58
CARMA-15	10.4	6.1	90	10	0.19	13	17	−45	69
CARMA-15	6.1	6.1	90	10	0.30	15	37	3	90
CARMA-23	10.4	10.4	86	10	0.22	14	15	−80	61
CARMA-23	10.4	6.1	86	10	0.14	14	16	−65	72
CARMA-23	6.1	6.1	86	10	0.26	15	37	4	94
CARMA-23	10.4	3.5	88	10	0.80	16	18	59	80
CARMA-23	6.1	3.5	88	10	0.76	11	17	−81	120
CARMA-23	3.5	3.5	88	5	2.64	31	68	−44	220

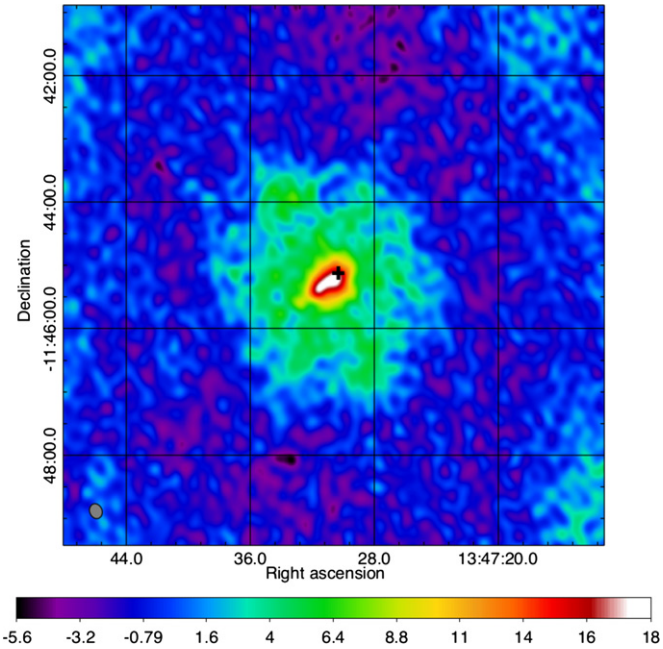

Figure 1. Dirty map of RX J1347.5−1145. In order to show both the large and small scale structure, we apply natural visibility weighting for visibilities with variances smaller than the mean and uniform weighting for the remainder. The position of the emissive source is marked in black. The map is in units of Compton $y \times 10^{13}$ beam^{-1}, where the beam is defined by a Gaussian fit to the main lobe and has a FWHM of $13\farcs7 \times 10\farcs9$ at position angle 32°, as shown in the gray ellipse in the lower left of the figure.

(A color version of this figure is available in the online journal.)

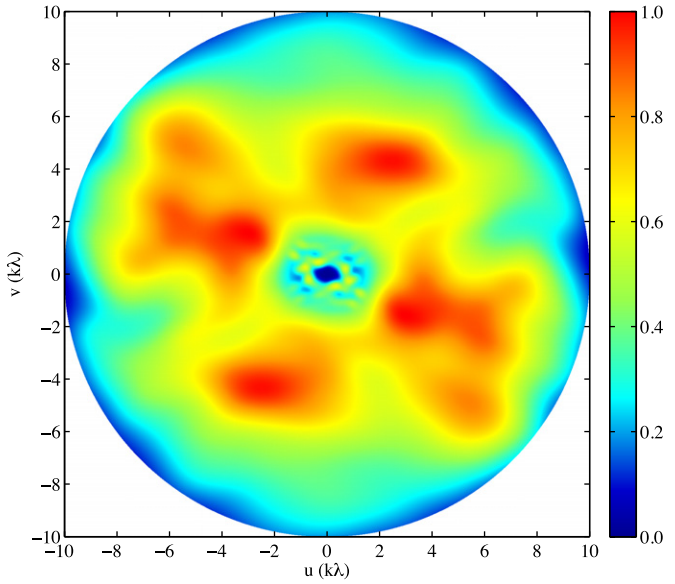

Figure 2. Normalized data weight distribution in the uv plane for the union of data sets described in Table 1. Weights are calculated from the inverse variance of each visibility, scaled by the SZ intensity spectrum. The uv-plane extent of each visibility weight is determined from the cross-correlation of the illumination patterns of the corresponding antennas, providing a more complete view of the uv sampling in the heterogeneous array. The weights are well-matched to the cluster signal—which is largest at small uv radius—except for a relatively undersampled region around ∼2 kλ. This region of the uv plane will be well-measured by the 23 element CARMA array at 1 cm, which is currently under development.

(A color version of this figure is available in the online journal.)

CARMA-8 at 1 cm constrains the cluster at small uv radius (large angular scale) where the signal is largest, while CARMA-15 and CARMA-23 at 3 mm are sensitive to the large uv radius (small angular scale) substructure of the cluster. The large CARMA-23 uncertainties at arcminute angular scales arise due to the reduced bandwidth and extensive flagging of the 3.5 m antennas mentioned above.

4. MODELING AND DECONVOLUTION

4.1. Method

We wish to use the information in our visibility data to determine the properties of the cluster. For low-resolution data such as that produced by CARMA-8, this is often accomplished by fitting the visibility data using an analytical model with a small number of free parameters (see, e.g., Carlstrom et al. 1996; Marrone et al. 2012). While this approach is useful for deriving bulk cluster properties under the assumption of self-similarity, it is not optimal for detailed imaging of morphologically complex clusters due to the difficulty in choosing an appropriate model. However, some sort of modeling or deconvolution technique is necessary to interpret the data due to the incomplete uv coverage and the primary beam attenuation. We take a very general approach, determining the point source emission directly from the visibilities and iteratively building a model of the cluster in the image plane as a superposition of Gaussians.

The bright emissive source at the center of the cluster, which we find to be consistent with a point source in our data, is modeled as a delta function with the flux, R.A., and decl. free to vary. The spectral index is fixed to zero across the band for each individual sub-array (CARMA-15, CARMA-23, and CARMA-8), but the flux is independently determined for each sub-array—since radio source fluxes often vary considerably with time, identical fluxes should not be expected in the

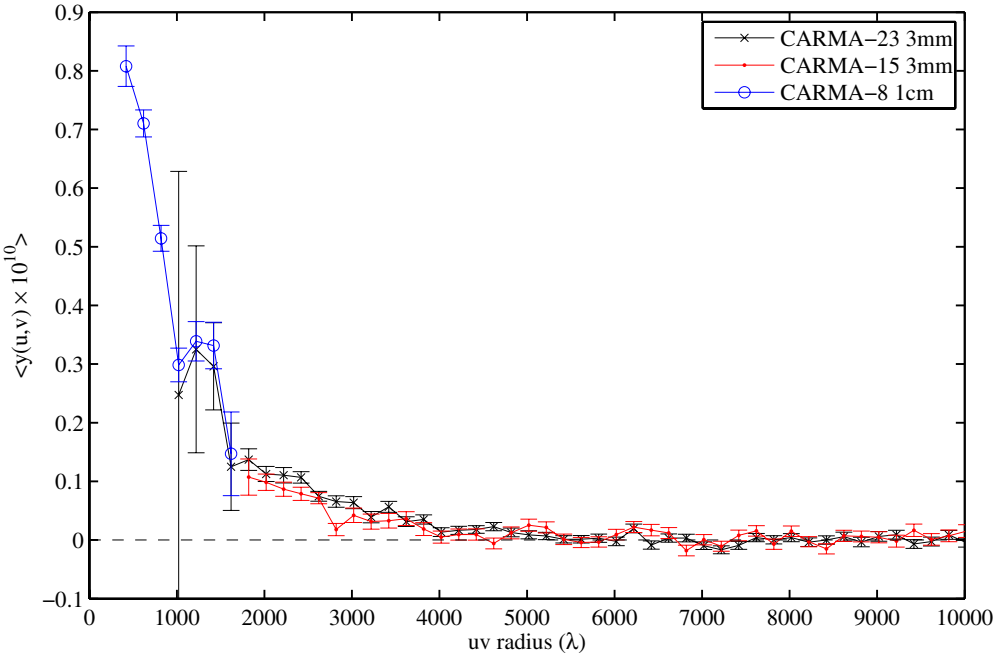

Figure 3. Radially binned visibilities from CARMA-8 at 1 cm, CARMA-15 at 3 mm, and CARMA-23 at 3 mm. The CARMA-8 data measure the cluster signal at large angular scales, while the other sub-arrays measure the smaller substructure of the cluster.

(A color version of this figure is available in the online journal.)

CARMA-15 and CARMA-23 despite their similar central frequencies. The position of the source is allowed to vary but is assumed to be the same for all sub-arrays. We find a best-fit position at an R.A. of 13:47:30.7 and a decl. of −11:45:09 (J2000), consistent with a source in the NVSS catalog (Condon et al. 1998). The flux of this source was found to be 8.8 ± 0.2 mJy in the 1 cm CARMA-8 data, 4.9 ± 0.1 mJy in the 3 mm CARMA-23 data, and 5.4 ± 0.3 mJy in the 3 mm CARMA-15 data. By way of comparison, the peak of the cluster signal in the point source-subtracted CARMA-8 dirty map is −7.6 mJy beam^{-1}. We subtract the best-fit point source models from the visibility data sets before proceeding.

We next apply a phase shift to the CARMA-15 visibilities to establish a single phase center for all 10 data sets. At this stage, all of the visibilities can be combined to form a single dirty map, which is shown in Figure 1 (though it is not used in our analysis). This map includes data with dramatically different primary beams. To account for this complication, we iteratively build a model from the ten dirty maps corresponding to each primary beam: CARMA-8 3.5 m × 3.5 m at 1 cm, CARMA-15 6.1 m × 6.1 m at 3 mm, and so on.

We begin by making a dirty map from the visibilities corresponding to the smallest primary beam, $y_1(u, v)$. We run the Högbom CLEAN algorithm (Högbom 1974) on this map with gain 0.05, stopping at 2.5σ, with a 48″ × 40″ CLEAN box encompassing the cluster core and substructure. The CLEAN components are corrected for the appropriate primary beam, and a restored map is generated. This restored map (in units of Compton y per pixel) is our initial cluster model. The cluster model is then multiplied by the primary beam of the next data set, $y_2(u, v)$, and the result is Fourier transformed and subtracted from $y_2(u, v)$. From these model-subtracted visibilities, a dirty map is produced and Högbom CLEANed. The CLEAN components are corrected for the primary beam and restored, and the restored map is added to the cluster model. We repeat this process on all ten data sets, resulting in a cluster model that incorporates information from all of our data. We continue refining the model by making additional passes through all ten data sets until each model-subtracted dirty map is consistent with noise. Three iterations are found to be sufficient. Our final cluster model is then added to the weighted average of the 10 model-subtracted dirty maps to form a CLEAN map (Figure 4).

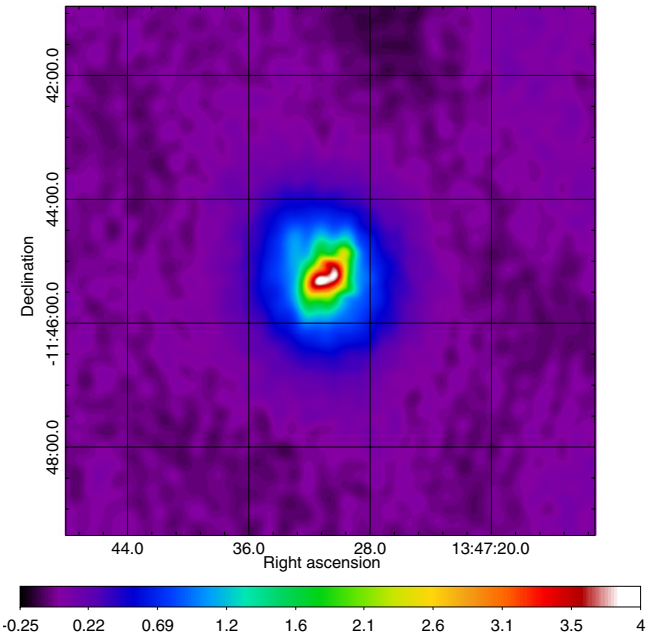

Figure 4. CLEAN map of RX J1347.5−1145. The map is in units of Compton $y \times 10^{15}$ pixel^{-1}, where the pixel size is 0.″5 × 0.″5. The smallest CLEAN beam used to construct the model is 11″ × 17″.

(A color version of this figure is available in the online journal.)

Due to the different primary beam patterns of the individual sub-arrays, the resolution of the map varies as a function of

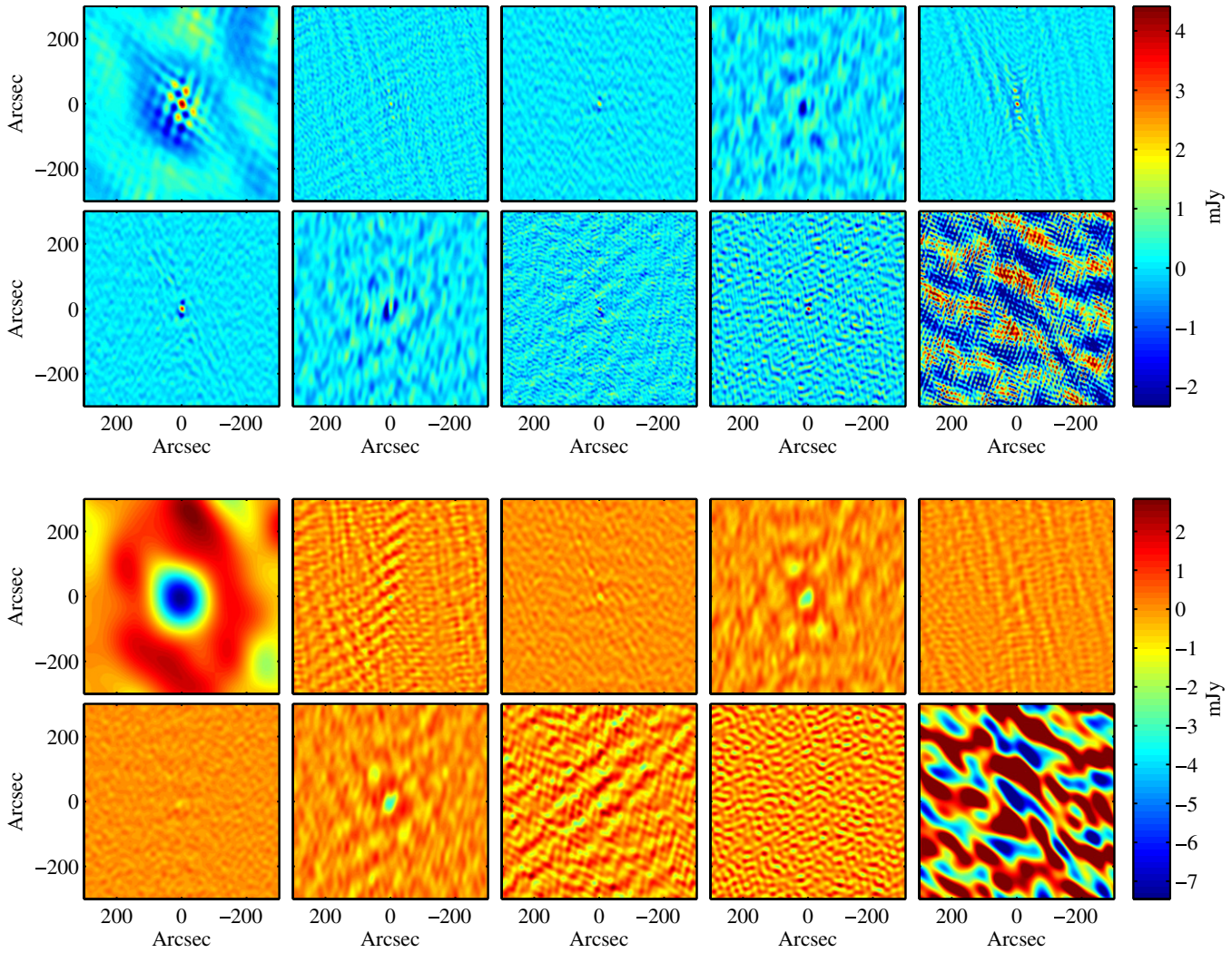

Figure 5. Dirty maps for each of the 10 CARMA data sets before point source subtraction and uv radius cut (above), and after (below). From top left to bottom right, both sets of maps are ordered as follows: CARMA-8 at 31 GHz; CARMA-15 at 90 GHz 10.4 m × 10.4 m, 10.4 m × 6.1 m, and 6.1 m × 6.1 m; and CARMA-23 at 86 GHz 10.4 m × 10.4 m, 10.4 m × 6.1 m, 6.1 m × 6.1 m, 10.4 m × 3.5 m, 6.1 m × 3.5 m, and 3.5 m × 3.5 m. The color scale is in units of mJy beam^{-1}.
(A color version of this figure is available in the online journal.)

position. The smallest angular scale recovered at a given position is set by the smallest restoring beam for which the corresponding primary beam is non-negligible at that position. For example, within the 118″ FWHM primary beam of the 10.4 m × 3.5 m sub-array (pointed directly at the cluster center), the resolution is 17″ × 11″. The noise level, beam size, and beam position angle (P.A.) are shown in Table 1, and the 10 single sub-array dirty maps are shown in Figure 5.

4.2. Verification

To assess the accuracy and flux recovery of our deconvolution technique, we repeat the process described above using a simulated RX J1347.5−1145 SZ signal. Simulating the SZ signal requires knowledge of the ICM density n_e and temperature T_e, both of which can be approximated using the results of Allen et al. (2002, hereafter A02) derived from *Chandra* X-ray data. For the electron density, we use the A02 β-model density fit within the central region and a power law with an index of −2.331 in the outer region (the latter is inferred from the A02 surface brightness profile fit). We piece together the inner and outer regions by requiring that $n_e(r)$ be continuous. For the electron temperature, we use the A02 measured temperature profile out to the outer radius of their largest bin, and use the average temperature of 12.0 keV at larger radius. We assign a temperature of 18.0 keV in the shocked region of the southeast quadrant. Finally, we truncate both the temperature and density profiles at r_{200}.

Using these approximations for the electron density and temperature, we integrate along the line of sight to produce a simulated Compton y map, Fourier transform, and sample at the measured (u, v) coordinates to produce simulated visibilities $y_{\rm sim}(u, v)$. We then randomize the phases in our visibility data $y(u,v)$ to produce simulated noise $y_{\rm noise}(u, v)$. The sum of the signal and noise $y_{\rm sim}(u, v) + y_{\rm noise}(u, v)$ yields simulated data identical to the measured data in its (u, v) sampling and noise properties. We then run our iterative deconvolution routine on the simulated data and compare the results to the input model (see Figure 6). Our algorithm accurately reproduces the locations and relative amplitudes of the bulk cluster emission and the disturbed region, and recovers 69%, 78%, and 92% of the total integrated flux within r_{200}, r_{500}, and r_{2500} (where the r_Δ values are determined from the Allen et al. 2002 NFW model fit). By repeating the simulation with different noise realizations,

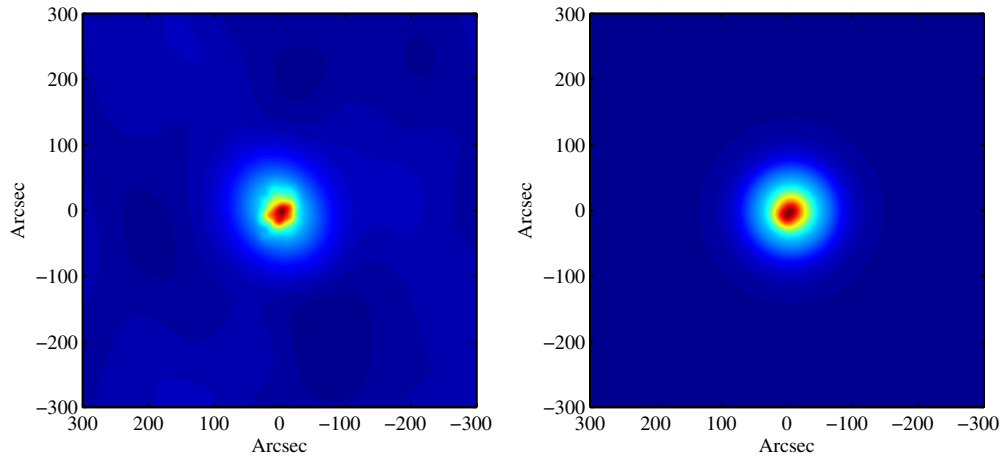

Figure 6. Left: a simulated CARMA map of an RX J1347.5−1145-like cluster using the technique described in this work. Right: the simulated cluster convolved with the smallest of the ten sub-array CLEAN beams.

(A color version of this figure is available in the online journal.)

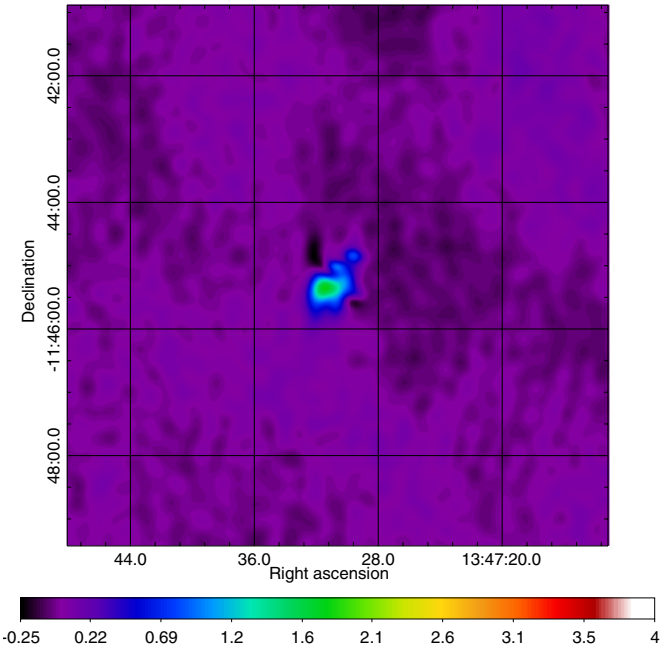

Figure 7. CLEAN map of RX J1347.5−1145 with the scaled relaxed X-ray pressure profile subtracted from the visibilities. The map is in units of Compton $y \times 10^{15}$ pixel^{-1}, where the pixel size is $0\farcs5 \times 0\farcs5$.

(A color version of this figure is available in the online journal.)

we found that the statistical uncertainty in the recovered flux is 3.5%.

The free morphological parameters in our simulated model include the β-model core radius and β, the electron density power law index at larger radii, and the transition radius between the two regimes. We varied each parameter and re-ran our analysis, and found that the transition radius and the outer power law index had the most impact on flux recovery, with a 10% variation in each of these parameters resulting in a ∼6% change in the recovered flux. For all four parameters, changes resulting in a more compact cluster resulted in increased flux recovery. For example, a shallow power law index would add additional SZ signal extending to radii beyond r_{200} ($5\farcm75$ for this cluster), which corresponds to angular scales larger than can be measured by the shortest CARMA baselines.

To verify the accuracy of our point source removal, we added 25 and 50 mJy emissive point sources in the center of the simulated cluster and removed them using the same technique applied to the real data. We found that the inclusion of these sources affected our recovered flux by ∼1%, which is below the 3.5% statistical uncertainty.

5. RESULTS

The iteratively deconvolved map of RX J1347.5−1145 shown in Figure 4 is reminiscent of a relaxed cluster SZ signal with additional sub-arcminute structure in the southeast quadrant imparted by the merger event. The imaging of both the extended and compact structure in our SZ map is of extremely high fidelity due to our ability to remove the central point source and to the large angular dynamic range of the combined arrays. In contrast with previous work (Mason et al. 2010; Komatsu et al. 2001), we find that the peaks of the SZ and X-ray signals are coincident; the peak is likely suppressed in the single dish maps by the point source emission. Outside the region affected by the point source, we find broad agreement with Mason et al. (2010) on the morphological features of the cluster: a region of bright emission in the southeast, a smaller enhancement of the signal in the northwest, and a slight ellipticity of the bulk SZ signal (more extended in declination than in R.A.). We also find possible signatures of the enhanced SZ signal to the southwest of the cluster peak reported by Kitayama et al. (2004), as best seen in Figure 7. Figure 8 shows a comparison between the CARMA SZ map and the *Chandra* X-ray pressure map (Bradač et al. 2008). Though a full multi-wavelength reconstruction is beyond the scope of this paper, the two techniques clearly produce maps with consistent morphologies.

To separate the relaxed and disturbed components, we make use of the pressure profile fit to the *Chandra* X-ray data described in Allen et al. (2008), which excises the disturbed region in the southeast quadrant. Due to the depth of the *Chandra* data and the high X-ray luminosity of the target, the X-ray pressure profile is constrained out to 0.928 Mpc. We first project the pressure profile along the line of sight to produce an integrated pressure map. For each sub-array, we multiply this map by the appropriate primary beam, convert to Compton y, Fourier transform, and subtract the result from the visibility data. We then iteratively build a model of the remaining SZ signal,

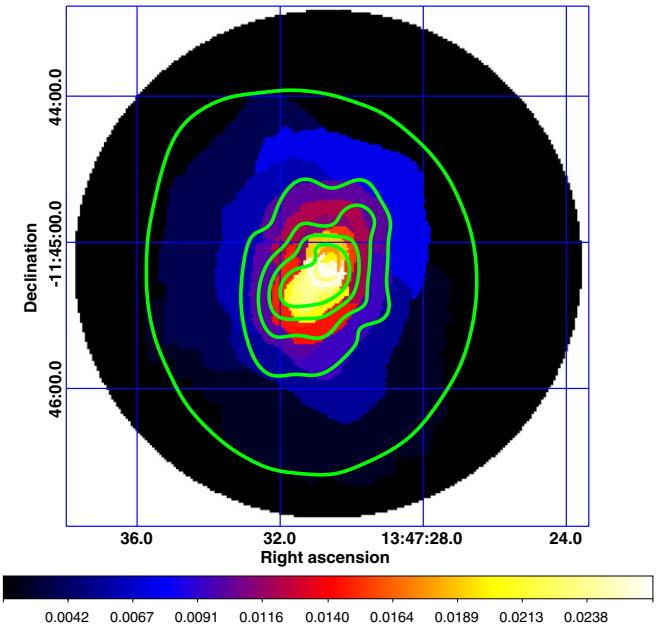

Figure 8. X-ray-derived integrated pressure map from Bradač et al. (2008) with CARMA SZ contours overlaid. Contours are in units of $y \times 10^{15}$ pixel^{-1} in increments of 0.7 starting at −0.25, while the color scale is in units of keV cm$^{-5/2}$ arcsec^{-1}.

(A color version of this figure is available in the online journal.)

following the procedure described in Section 4. We allow the X-ray pressure profile to be scaled by a multiplicative constant to compensate for cluster projection effects and calibration errors. The scale factor is chosen to produce the minimum total 31 GHz CARMA-8 (arcminute-scale) signal in the iteratively-determined model.

Removing this estimate of the relaxed signal from our visibility data allows us to focus on the sub-arcminute-scale signal resulting from the merger event. The result is shown in Figure 7. The total Compton y signal recovered in this map, which corresponds to the fraction of the thermal energy in the cluster ICM associated with the merger-related substructure, is 9.1% ± 1.4% of the total recovered from the map in Figure 4. This value is consistent with the MUSTANG analysis of Mason et al. (2010).

We cross-checked this result by fitting a simple model directly to the visibility data. The model consisted of a point source with positions coupled between sub-arrays but with independent fluxes, as in Section 4, and two generalized NFW models (Nagai et al. 2007). The scale radii and normalizations of the generalized NFW components were allowed to vary and the power law indices were fixed to the values in Arnaud et al. (2010). The model is a poor fit (reduced χ^2 of 1.4 for 149,721 degrees of freedom), which is unsurprising given the complex morphology of the cluster, and the errors on the parameter values are correspondingly large. Nevertheless, total integrated Y parameter within $r_{2500} = 61$ Mpc (Allen et al. 2002, converted to our cosmology) is well-constrained: $Y D_A^2 = 10.4 \pm 0.3 \times 10^{-5}$ Mpc^2. Moreover, the percentage of the total integrated Y contributed by the smaller generalized NFW component is consistent with the iteratively determined value: $9.0^{+2.1}_{-4.9}$%.

The value of the multiplicative constant by which the X-ray pressure is scaled can also yield information about the characteristics of the cluster. Since the scale factor is determined by requiring consistency with the CARMA-8 data, its value depends upon the three-dimensional morphology of the ICM on large angular scales. Due to the different dependencies of the X-ray surface brightness and the SZ signal on density, a cluster more (less) extended along the line of sight than in the plane of the sky would yield a scale factor of greater than (less than) one (see, e.g., Grego et al. 2004). For this cluster, we find a scale factor of 0.588 ± 0.012, where the error bar encompasses the range of scale factors producing a peak 31 GHz CARMA-8 signal of ±1× the map rms. If all other effects are assumed sub-dominant, this value would imply that RXJ 1347.5−1145 is strongly compressed along the line of sight. A similar ratio is reported in Bonamente et al. (2011) using the CARMA-8 data reported here. Chakrabarty et al. (2008), using a combination of X-ray and SZ data, find that RX J1347.5−1145 is compressed along the line of sight with an axis ratio of ∼5. A simple comparison of the X-ray surface brightness profile and our data, assuming an isothermal cluster, implies compression along the line of sight by a factor of roughly three-to-one—a fairly extreme value, though less than suggested by Chakrabarty et al. (2008).

Clumping of the ICM, i.e., a systematic discrepancy between $\langle n_e^2(r)\rangle$ and $\langle n_e(r)\rangle^2$, could also lead to differences between the SZ and X-ray signals. Clumping is observed in the outskirts of simulated clusters (Nagai & Lau 2011), and is implied by observations of flattened entropy profiles and gas mass fractions apparently in excess of the cosmic mean in some clusters (e.g., Simionescu et al. 2011). However, in both cases the clumping occurs at large cluster radii (at least $>r_{500}$), and is thus unlikely to affect the normalization of the X-ray model used here (which was fit to data at $r < r_{500}$) at the level required to explain the offset.

The ∼40% difference between the CARMA and *Chandra* pressure estimates could also arise in principle from calibration or systematic errors in the X-ray or SZ data. However, Allen et al. (2008) report $\lesssim$10% calibration and systematic errors, and recent refinements to the *Chandra* spectroscopic calibration have been at the ∼10% level (see, e.g., Reese et al. 2010). As discussed in Section 3, the CARMA calibration is expected to be accurate to with 5%; a 40% error in the arcminute angular scale signal would require a gross mis-calibration of the CARMA-8 data. To check for such an error, we compared our data with BIMA observations of RX J1347.5−1145 described in Bonamente et al. (2008). These data were gathered, reduced, and calibrated in a completely independent manner from CARMA-8. We jointly fit the two visibility data sets using a generalized NFW model, constraining the ratio of the pressure normalizations while marginalizing over the point source parameters as well as the cluster scale radius and position. The ratio of the CARMA-8 to the BIMA pressure normalization is found to be 1.17 ± 0.13, providing evidence against a 40% low CARMA-8 calibration.

Since major mergers such as RX J1347.5−1145 are not expected to be spherically symmetric, we suggest that line-of-sight compression is most likely to be the dominant effect. However, both ICM clumping and calibration errors may also be contributing to the discrepancy at the ∼10%–20% level. A more complete explanation will require joint analysis of the X-ray and SZ data.

6. CONCLUSIONS AND FUTURE WORK

We have demonstrated the ability of CARMA to measure the SZ signature of galaxy clusters at high sensitivity across a wide

range of angular scales. By combining data from three CARMA configurations and two frequency bands, we measure both the arcminute-scale signal and the ten-arcsecond-scale substructure of RX J1347.5−1145 while constraining and removing the effects of the associated emissive point source. By comparing our data to the X-ray measurements of Allen et al. (2008), we are able to determine that ∼9% of the SZ signal is localized in the disturbed region of the cluster, and that the system is likely compressed along the line of sight relative to the plane of the sky.

Although our results demonstrate that CARMA in its current form is a highly capable SZ instrument, several upgrades will soon bring about significant enhancements. An effort is currently underway to equip all antennas with 1 cm receivers and expand the correlator bandwidth to 8 GHz for the 23 element array. The 3 mm CARMA-23 array described in this work provided sensitivity from uv radii of ∼2.0 to 10 kλ; the upgraded array placed in the same configuration but operated at 1 cm will provide enhanced sensitivity from ∼0.35 to 3.3 kλ. As shown in Figure 3, this corresponds to the portion of the uv plane where the SZ signal is large. A planned upgrade to more the 3 mm receivers will further increase the sensitivity of the array to finer angular scale SZ signals.

Since the primary beams of the larger CARMA telescopes do not always cover an entire galaxy cluster, smaller angular scale SZ structures can be measured in specific regions of interest, as was done in this study by pointing them toward the region of hot gas to the southeast of the cluster center. With the increased sensitivity enabled by the ongoing upgrades, this technique can be used to search for shock-enhanced features in the outskirts of clusters. Mosaicking can also be used to provide sensitivity to small-scale structures over the entire cluster.

Taken together, these upgrades and observing strategies will allow CARMA to image clusters precisely and efficiently over a wide angular dynamic range, making it possible to fully exploit the power of the SZ effect as a probe of cluster astrophysics and precision cosmology.

We thank Evan Million for providing the X-ray pressure data from Bradač et al. (2008), and Steve Allen for providing the X-ray fit from Allen et al. (2008). We also thank Maruša Bradač and Myriam Gitti for useful discussions.

Support for CARMA construction was derived from the Gordon and Betty Moore Foundation, the Kenneth T. and Eileen L. Norris Foundation, the James S. McDonnell Foundation, the Associates of the California Institute of Technology, the University of Chicago, the states of California, Illinois, and Maryland, and the National Science Foundation. Ongoing CARMA development and operations are supported by the National Science Foundation under a cooperative agreement, including grant AST-0838187 at the University of Chicago, and by the CARMA partner universities. Partial support is provided by NSF Physics Frontier Center grant PHY-1125897 to the Kavli Institute of Cosmological Physics. D.P.M. was supported for part of this work by NASA through Hubble Fellowship grant HST-HF-51259.01.

Finally, we thank the CARMA staff for making the 23 element commissioning observations possible.

Facility: CARMA.

REFERENCES

Allen, S. W., Rapetti, D. A., Schmidt, R. W., et al. 2008, MNRAS, 383, 879
Allen, S. W., Schmidt, R. W., & Fabian, A. C. 2002, MNRAS, 335, 256
Arnaud, M., Pratt, G. W., Piffaretti, R., et al. 2010, A&A, 517, A92
Bonamente, M., Hasler, N., Bulbul, E., et al. 2011, NJPh, 14, 025010
Bonamente, M., Joy, M., LaRoque, S. J., et al. 2008, ApJ, 675, 106
Bradač, M., Schrabback, T., Erben, T., et al. 2008, ApJ, 681, 187
Carlstrom, J. E., Holder, G. P., & Reese, E. D. 2002, ARA&A, 40, 643
Carlstrom, J. E., Joy, M., & Grego, L. 1996, ApJL, 456, L75
Chakrabarty, D., de Filippis, E., & Russell, H. 2008, A&A, 487, 75
Cohen, J. G., & Kneib, J.-P. 2002, ApJ, 573, 524
Condon, J. J., Cotton, W. D., Greisen, E. W., et al. 1998, AJ, 115, 1693
Gitti, M., Ferrari, C., Domainko, W., Feretti, L., & Schindler, S. 2007, A&A, 470, L25
Gitti, M., & Schindler, S. 2004, A&A, 427, L9
Grego, L., Vrtilek, J. M., Van Speybroeck, L., et al. 2004, ApJ, 608, 731
Högbom, J. A. 1974, A&AS, 15, 417
Johnson, R. E., ZuHone, J. A., Jones, C., Forman, W., & Markevitch, M. 2011, ApJ, 751, 95
Kitayama, T., Komatsu, E., Ota, N., et al. 2004, PASJ, 56, 17
Komatsu, E., Matsuo, H., Kitayama, T., et al. 2001, PASJ, 53, 57
Korngut, P. M., Dicker, S. R., Reese, E. D., et al. 2011, ApJ, 734, 10
Malu, S. S., Subrahmanyan, R., Wieringa, M., & Narasimha, D. 2010, arXiv:1005.1394
Marrone, D. P., Smith, G., Okabe, N., et al. 2012, ApJ, 754, 119
Mason, B. S., et al. 2010, ApJ, 716, 739
Miranda, M., Sereno, M., de Filippis, E., & Paolillo, M. 2008, MNRAS, 385, 511
Muchovej, S., Mroczkowski, T., Carlstrom, J. E., et al. 2007, ApJ, 663, 708
Nagai, D., Kravtsov, A. V., & Vikhlinin, A. 2007, ApJ, 668, 1
Nagai, D., & Lau, E. T. 2011, ApJL, 731, L10
Pointecouteau, E., Giard, M., Benoit, A., et al. 1999, ApJL, 519, L115
Reese, E. D., Kawahara, H., Kitayama, T., et al. 2010, ApJ, 721, 653
Rudy, D. J. 1987, PhD thesis, California Institute of Technology
Sault, R. J., Teuben, P. J., & Wright, M. C. H. 1995, in ASP Conf. Ser. 77, Astronomical Data Analysis Software and Systems IV, ed. R. A. Shaw, H. E. Payne, & J. J. E. Hayes (San Francisco, CA: ASP), 433
Simionescu, A., Allen, S. W., Mantz, A., et al. 2011, Sci, 331, 1576
Voges, W., Aschenbach, B., Boller, Th., et al. 1999, A&A, 349, 389
Zemcov, M., Aguirre, J., Bock, J., et al. 2012, ApJ, 749, 114